



Cite this: *RSC Adv.*, 2017, 7, 22983

# Facile synthesis of a $\alpha$ -MoO<sub>3</sub> nanoplate/TiO<sub>2</sub> nanotube composite for high electrochemical performance†

Shupe Sun, Xiaoming Liao, \* Yu Sun, Guangfu Yin, Yadong Yao, Zhongbing Huang and Ximing Pu

A novel  $\alpha$ -MoO<sub>3</sub>/TiO<sub>2</sub> composite electrode material for high performance supercapacitor applications was synthesized using a facile electrodeposition technique. The surface morphology, microstructure, chemical composition and chemical states of the electrode material were analyzed using scanning electron microscopy, X-ray diffraction, energy dispersive X-ray spectroscopy, and X-ray photoelectron spectroscopy. Cyclic voltammetry tests, galvanostatic charge–discharge measurements, and electrochemical impedance spectroscopy were employed to analyze electrochemical behavior. The results demonstrate that a very high capacitance (43.42 mF cm<sup>−2</sup>) can be achieved at a scan rate of 20 mV s<sup>−1</sup> in 1 M aqueous Na<sub>2</sub>SO<sub>4</sub> solution and good capacitance behavior even after 3000 continuous charge–discharge cycles, indicating potential applications as an electrode material for supercapacitors.

Received 26th January 2017  
Accepted 5th April 2017

DOI: 10.1039/c7ra01164d

rsc.li/rsc-advances

## 1. Introduction

Over the past few years, extensive studies have focused on the development of new electrode materials for advanced energy storage devices,<sup>1–6</sup> due to the ever-increasing power and energy requirements in the modern electronics industry. Among the various energy-storage devices, electrochemical capacitors (EC), also called supercapacitors, are one of the most promising electrochemical energy-storage systems and have attracted tremendous attention. Generally, according to the charge/discharge mechanism, supercapacitors can be classified into two categories: electrical double-layer capacitors (EDLCs), which commonly use carbon-active materials (activated carbon,<sup>7,8</sup> carbon nanotubes,<sup>9,10</sup> and graphene<sup>11,12</sup>), and pseudocapacitors, which use transition metal oxides/sulfides (RuO<sub>2</sub>,<sup>13,14</sup> NiO<sub>x</sub>,<sup>15,16</sup> MnO<sub>x</sub>,<sup>17,18</sup> CoS,<sup>19</sup> ZnS,<sup>20</sup> etc.) and conducting polymers (e.g. polypyrrole,<sup>21–23</sup> polyaniline<sup>24,25</sup>). Among the different transition metal oxides, titanium dioxide (TiO<sub>2</sub>)<sup>26,27</sup> and molybdenum oxide (MoO<sub>3–x</sub>)<sup>28–35</sup> have received immense interest for applications in electrode materials, due to their low cost, low toxicity, natural abundance, and environmentally friendly nature.

Self-assembled titania nanotubes (TNTs) can be easily fabricated by one-step anodization of Ti sheets in a two-electrode system in fluoride-containing electrolytes.<sup>15–20</sup> The highly ordered structure and large surface area of TNTs increase

reaction sites as well as promote charge and ions transfer, enhancing supercapacitor performance of composite electrode. Therefore, many researches employ TNTs as a substrate and construct composite electrode material. Zhou *et al.* achieved MnO<sub>2</sub>–TiO<sub>2</sub> composite electrode *via* a sequential chemical bath deposition.<sup>18</sup> Ray *et al.* fabricated titania nanotube/cobalt sulfide composite electrode by electrochemical technique.<sup>19</sup> Du *et al.* prepared polypyrrole–titania nanotube hybrid through a normal pulse voltammetry deposition process.<sup>22</sup> Xie *et al.* prepared polypyrrole/titania/polyaniline coaxial nanotube hybrid through an electrodeposition process.<sup>21</sup> In conclusion, transition metal oxide or conducting polymer incorporated with TNTs exhibited superior electrochemical performance resulted from their synergistic effect.

MoO<sub>3</sub> has attracted considerable attention as a promising transition metal oxide widely used in the fields of photochromic and electrochromic devices,<sup>33</sup> gas sensors,<sup>34</sup> and energy storage.<sup>28–30</sup> There are three basic polytypes of MoO<sub>3</sub>, orthorhombic MoO<sub>3</sub> ( $\alpha$ -MoO<sub>3</sub>), monoclinic MoO<sub>3</sub> ( $\beta$ -MoO<sub>3</sub>), and hexagonal MoO<sub>3</sub> (h-MoO<sub>3</sub>). Among them,  $\alpha$ -MoO<sub>3</sub> has received immense attention because of its unique layer structure.<sup>28,30,32</sup> The unique structure allows atoms, ions or molecules to be introduced into the layers through intercalation.  $\alpha$ -MoO<sub>3</sub> also has a high theoretical capacity of 1111 mA h g<sup>−1</sup>,<sup>36</sup> almost three times that of the graphite.<sup>37</sup> Li *et al.* studied the electrochemical behavior of  $\alpha$ -MoO<sub>3</sub> nanobelts deposited on a foam nickel plate, whose specific capacitance was as high as 280 F g<sup>−1</sup>.<sup>28</sup> Sarfraz *et al.* reported the electrochemical performance of MoO<sub>3</sub> nanowires coated onto a conductive carbon cloth, which exhibited a high specific capacitance of 288 F g<sup>−1</sup>.<sup>29</sup> Compared to foam nickel plate or carbon cloth, the well-aligned nanotubes

College of Materials Science and Engineering, Sichuan University, Chengdu, Sichuan 610065, China. E-mail: sherman\_xm@163.com; Fax: +86 28 85413003

† Electronic supplementary information (ESI) available. See DOI: 10.1039/c7ra01164d



vertically oriented from the surface of Ti substrate, as current collector, do not need polymer binder and conductive additives. Additionally, Liu *et al.*<sup>38–40</sup> pointed out that 3D architecture nanocomposites contributed to achieving high-performance, low-cost and safe energy storage devices. Hence, we fabricated  $\alpha$ -MoO<sub>3</sub> nanoplates/TiO<sub>2</sub> nanotubes composite *via* a facile electrochemical deposition on nanotube surface and extensively studied its application for supercapacitor.

In this work, anatase TNTs were prepared by anodization and subsequent thermal treatment. Electrodeposition in molybdenum salt solutions was performed on as-prepared nanotube arrays and bare Ti sheets to obtain amorphous coatings, which then were transformed into the crystalline phase upon annealing in air. We compared the electrochemical behavior of molybdenum trioxide coated on TNTs and Ti metal. Our results demonstrate that these TNTs could be an excellent substrate and MoO<sub>3</sub>/TiO<sub>2</sub> is a promising electrode material.

## 2. Experimental procedure

### 2.1. Materials

The titanium sheet (TA2, purity > 99.6%, thickness 1 mm) was purchased from LuoKe titanium Ltd. Ethylene glycerol (C<sub>2</sub>H<sub>6</sub>O<sub>2</sub>, purity > 99.5%), ammonium fluoride (NH<sub>4</sub>F, purity > 96%) and hexaammonium molybdate tetrahydrate ((NH<sub>4</sub>)<sub>6</sub>Mo<sub>7</sub>O<sub>24</sub>·4H<sub>2</sub>O, purity > 99.0%) were purchased from KeLong Chemical Ltd. Other chemical reagents used in these experiments were of analytical grade and were used directly without further purification. All aqueous solutions were prepared using deionized water.

### 2.2. Fabrication of MoO<sub>3</sub>/TiO<sub>2</sub>

Highly ordered titania nanotubes (TNTs) were fabricated by one-step anodization of Ti sheets in ethylene glycerol containing 0.3 wt% NH<sub>4</sub>F and 6 vol% deionized H<sub>2</sub>O at 50 V for 30 min. A calcination treatment at 450 °C for 1 h was used to obtain crystalline TNTs, which are referred as TNT. Then electrochemical deposition of MoO<sub>3</sub> onto TNTs was carried out with a three-electrode system composed of annealed TNTs as the working electrode, a Pt foil as the counter electrode and an Ag/AgCl as the reference electrode. The deposition was performed in 0.05 M (NH<sub>4</sub>)<sub>6</sub>Mo<sub>7</sub>O<sub>24</sub>·4H<sub>2</sub>O aqueous solution by cycling from −0.6 to 0 V with a scan rate of 20 mV s<sup>−1</sup> for 17 cycles. The as-deposited TNTs are designated as AMO-TNT, which were then annealed in air at 450 °C for 1 h to obtain crystalline MoO<sub>3</sub>-coated nanotubes (CMO-TNT). For comparison, a MoO<sub>3</sub> film was directly grown by electrodeposition on Ti sheets *via* 17 cycles and then heat-treated at 450 °C for 1 h, which is referred as CMO-T.

### 2.3. Materials characterization and electrochemical measurements

The surface morphology and microstructure of the fabricated samples were investigated by scanning electron microscopy (SEM, Hitachi S4800, Japan), X-ray diffraction (XRD, X'Pert Pro MPD, Holland), respectively. Chemical composition of prepared

samples was characterized by an energy dispersive X-ray spectroscope (EDS, Oxford) attached on SEM. An X-ray photoelectron spectroscope (XPS, Escalab 250Xi, USA) was employed to analyze chemical states of the coating film. Electrochemical measurements were performed in a 1 M Na<sub>2</sub>SO<sub>4</sub> aqueous solution with an electrochemical workstation (CHI660E, China). Cyclic voltammetry (CV) tests were conducted over a potential voltage range from −0.9 to −0.2 V (*vs.* Ag/AgCl) at different scan rates (from 10 to 200 mV s<sup>−1</sup>). The galvanostatic charge-discharge (CD) testing was performed under different current densities (from 0.4 to 1 mA cm<sup>−2</sup>). Electrochemical impedance spectroscopy (EIS) measurements were conducted over a frequency range of 0.01 Hz to 100 kHz at an AC voltage amplitude of 5 mV. The cycling stability of the samples was tested by galvanostatic CD measurement performed up to 3000 cycles at a current density of 0.6 mA cm<sup>−2</sup>.

## 3. Results and discussion

### 3.1. Morphology and structure analyses

Fig. 1 shows the XRD patterns obtained over 2 $\theta$  range of 10° to 80° from TNT, CMO-T, AMO-TNT, and CMO-TNT. The peaks centered at  $\sim$ 25.2° and  $\sim$ 47.8° are the characteristic peaks of anatase TiO<sub>2</sub> (JCPDF 21-1272) while peaks at  $\sim$ 38.3° and  $\sim$ 40.1° are assigned to Ti (JCPDF 44-1294).<sup>18</sup> After deposition and thermal treatment, the pattern exhibits new peaks. The peaks with 2 $\theta$  of  $\sim$ 12.6°,  $\sim$ 25.5° and  $\sim$ 27.2° are indexed to orthorhombic  $\alpha$ -MoO<sub>3</sub> (JCPDF 05-0508).<sup>28</sup> However, there is no diffraction peak of  $\alpha$ -MoO<sub>3</sub> from the pattern of AMO-TNT, indicating deposition of amorphous molybdenum oxides onto anatase TiO<sub>2</sub> nanotubes.<sup>41</sup> We can observe the peaks of MoO<sub>3</sub> from the patterns of CMO-T and CMO-TNT, suggesting the formation of crystalline  $\alpha$ -MoO<sub>3</sub> phase after annealing at 450 °C for 1 h.

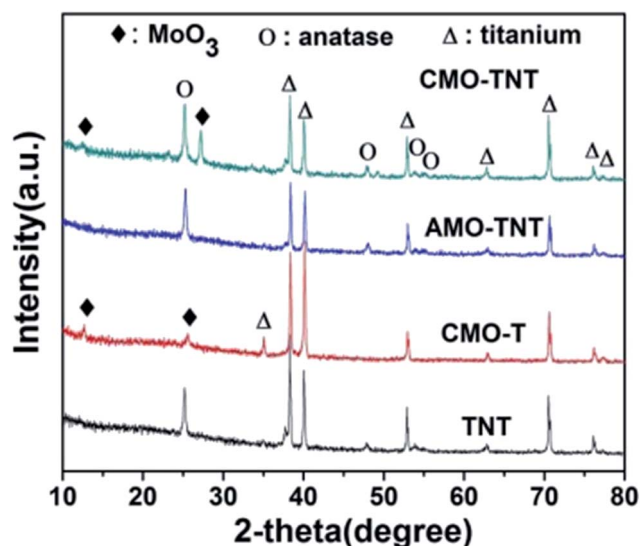


Fig. 1 XRD patterns of the samples TNT, AMO-TNT, CMO-TNT and CMO-T.



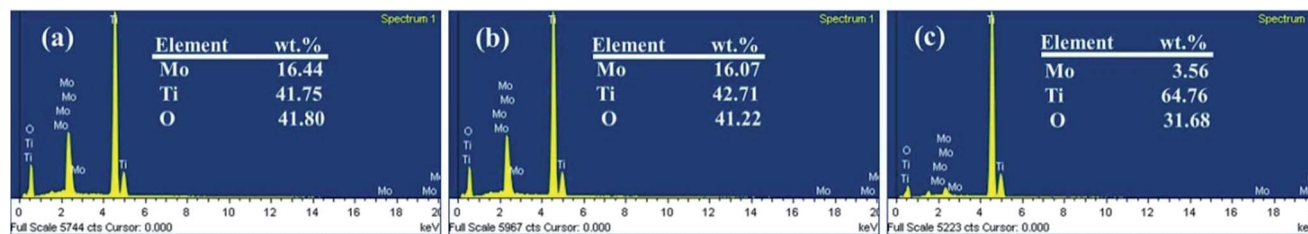


Fig. 2 EDS spectra of the samples CMO-TNT (a), AMO-TNT (b), and CMO-T (c).

An EDS analysis was also made to claim the presence of Mo elements. Fig. 2 shows the EDS spectra in which Mo, Ti and O elements are detected, suggesting formation of molybdenum oxide layer. In addition, there is no significant change in the amount of Mo from CMO-TNT when compared to AMO-TNT. The results confirm that annealing in the ambient environment after electrochemical deposition does not decrease the amount of  $\text{MoO}_3$ . However, the Mo amount of CMO-T is lower than that of AMO-TNT and CMO-TNT, indicating that TNTs substrate can contribute to the deposition of Mo.

Fig. 3 shows the surface morphology of TNT, CMO-T, AMO-TNT and CMO-TNT. The anodized TNTs (Fig. 3a) have open-top and uninterrupted nanotube structure which contribute to accessible surface area and promote the speedy permeation of electrolyte ions. Fig. 3b presents SEM image of AMO-TNT. Compared to TNT, there is a coating layer on the top of nanotubes and the precipitates are confirmed to be molybdenum oxides by EDS spectra. After heat treatment, the coating layer (Fig. 3c) becomes roughened. It is evident to see a large number of nanoplates aggregate with each other. From the results of XRD patterns, the coated layer is confirmed to be crystalline  $\text{MoO}_3$ . For a comparative study, planar Ti substrate was treated with electrochemical process to deposit  $\text{MoO}_3$  species. The dense film is confirmed to be orthorhombic molybdenum

trioxide. It should be noted that morphological difference is appeared between the CMO-TNT and CMO-T, *i.e.*, the smaller  $\text{MoO}_3$  nanoplates and more pores could be seen in the former samples compared to the latter prepared with the same method.

In our study, we discover the amount and morphological difference of  $\text{MoO}_3$  layer between CMO-TNT and CMO-T, which is attributed to the effect of nanotube arrays. On the one hand, the unique nanotube structure of anodized TNTs provide large surface area for absorbing more precursors and providing more nucleation points for  $\text{MoO}_3$  nanoplates compared to the planar Ti substrate.<sup>18</sup> On the other hand, the rugged tubular opening of the TNTs substrate inhibits growth of  $\text{MoO}_3$  layer in two-dimensional direction, beneficial to achieving small nanoplates. Thus TNTs play an important role in the quality of coating material.<sup>16</sup> As a result, it is understood that the hollow nanotubes of TNTs not only provide unique electron transport pathways for electrochemical reactions, especially for the rapid transfer of  $\text{Na}^+$  and  $\text{H}^+$  in a fast charge-discharge process, but offer large surface area for deposition of  $\text{MoO}_3$  to obtain composite electrode material. We can anticipate that TNTs coated with  $\text{MoO}_3$  exhibit excellent electrochemical behavior.

Furthermore, XPS was employed to analyze the chemical states of the coating layer. Fig. 4a shows the typical XPS survey spectra of AMO-TNT electrode. The Mo 3d<sub>5/2</sub> peak at 233.1 eV

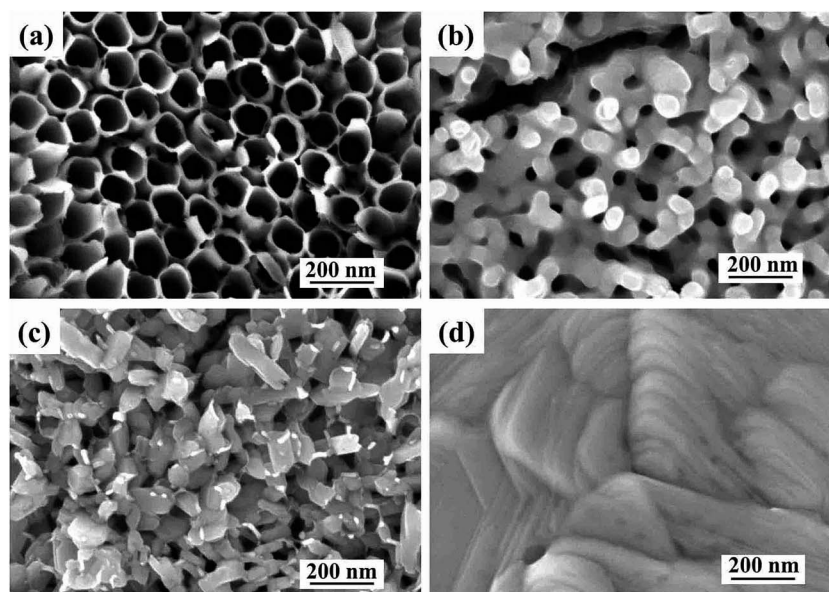


Fig. 3 SEM images of TNT (a), AMO-TNT (b), CMO-TNT (c) and CMO-T (d).





and the Mo 3d<sub>3/2</sub> peak at 236.3 eV correspond to Mo<sup>VI</sup>, and the Mo 3d<sub>5/2</sub> peak at 232.3 eV and the Mo 3d<sub>3/2</sub> peak at 235.6 eV correspond to Mo<sup>V</sup>.<sup>41,42</sup> As shown in Fig. 4b, the XPS spectrum shifting to high energies (Mo 3d<sub>5/2</sub> peak at 233.3 eV and the Mo 3d<sub>3/2</sub> peak at 236.5 eV) is assigned to  $\alpha$ -MoO<sub>3</sub>. As for the O 1s peak, a slight shift (0.2 eV) to a lower energy is observed, which is resulted from elimination of -OH groups and oxidation of Mo<sup>V</sup> ions during annealing process.<sup>43</sup> In summary, the composition of amorphous coating layer after electrochemical deposition is Mo<sup>V</sup> oxides and Mo<sup>VI</sup> oxides. Annealing in ambient environment leads to transition of amorphous molybdenum oxide to crystalline  $\alpha$ -MoO<sub>3</sub>. All in all, we successfully prepared  $\alpha$ -MoO<sub>3</sub>/TiO<sub>2</sub> composite electrode material through a facile electrodeposition method in molybdenum salt solutions.

### 3.2. Electrochemical characterizations

Electrochemical measurements were performed with a three-electrode system in 1 M Na<sub>2</sub>SO<sub>4</sub> electrolyte to evaluate the electrochemical performance of the MoO<sub>3</sub>/TiO<sub>2</sub> nanocomposite. For a comparison, the pristine TiO<sub>2</sub> nanotubes and MoO<sub>3</sub>/Ti substrate were also intensively studied. The CV curves for the TNT, CMO-T, AMO-TNT and CMO-TNT samples collected at a scan rate of 20 mV s<sup>-1</sup> are shown in Fig. 5a. The increased current of the CV curves for AMO-TNT and CMO-TNT clearly demonstrates improved electrochemical behavior after coating the nanotubes with MoO<sub>3</sub>. The Ti substrate coated MoO<sub>3</sub> film also exhibits low current response, resulting from its dense structure which is not beneficial to electrolyte ions diffusion. Compared to CMO-TNT, higher resistance at higher potentials of AMO-TNT indicates lower electroactivity, suggesting poorer capacitive behavior.<sup>44</sup> Furthermore, the area under CV curve for CMO-TNT is larger than that of other samples, implying enhanced electrochemical properties. The effect of different scan rates on the electrochemical behavior of CMO-TNT has been studied and the results are presented in Fig. 5b. All plots are close to an ideal rectangular shape without evident redox peaks, which is a typical character of double-layer capacitance. Additionally, the shapes of CV curves do not significantly change as the scan rate is increased to 0.2 V s<sup>-1</sup>, indicating good capacitive behavior and high-rate capability. Fig. 5c shows the

calculated areal capacitance of these electrodes as a function of scan rate. The specific capacitances are calculated by the following equation:

$$C_s = C/S = I/[(dV/dt) \times S] \quad (1)$$

The areal capacitances of TNT, CMO-T, AMO-TNT, and CMO-TNT are 2.97 mF cm<sup>-2</sup>, 2.55 mF cm<sup>-2</sup>, 35.67 mF cm<sup>-2</sup> and 43.42 mF cm<sup>-2</sup> at a scan rate of 20 mV s<sup>-1</sup>, respectively. For all of the samples, the specific capacitance decreases with increasing scan rate. Notably, the specific capacitance of the CMO-TNT remains as high as 31.60 mF cm<sup>-2</sup> at a high scan rate (0.2 V s<sup>-1</sup>), demonstrating better rate capability and ion transportation performance than the other investigated samples. The decay of the specific capacitance is attributed to the charge not being able to completely accumulate in the materials at high scan rates.

$\alpha$ -MoO<sub>3</sub> is known as a layered structure of [MoO<sub>6</sub>] octahedron. These layers are connected by weak van der Waals force containing van der Waals gaps which are favorable for intercalation of electrolyte ions and accommodate large quantities of positive ions.<sup>28,45,46</sup> Dunn and his coworkers<sup>47</sup> systematically study capacitance contribution of porous electrode. When the grain size decreases to nanoscale dimensions, there is some amount of charge stored from the insertion process. Thus, we propose that nanosize  $\alpha$ -MoO<sub>3</sub> plates with distinct layer structure are favorable of intercalation and deintercalation of electrolyte ions, and thus enhancing the electrochemical behavior. Additionally, the layered structure also offers superior charge transfer behavior.<sup>48</sup> The difference between AMO-TNT and CMO-TNT is attributed to the crystal structure and chemical states of molybdenum oxides, capacitive factors and electrochemical kinetics.<sup>49,50</sup> Therefore, if crystalline  $\alpha$ -MoO<sub>3</sub> is used as coating material, the hybrid electrode material will exhibit excellent electrochemical performance. The highly ordered and uninterrupted structure of TNTs not only provides large surface area and direct pathways, but also helps to make best utilization of nanosized  $\alpha$ -MoO<sub>3</sub> and promote charge transfer inside a porous electrode. There is no doubt that TNTs have a progressive and positive influence on the capacitive behavior

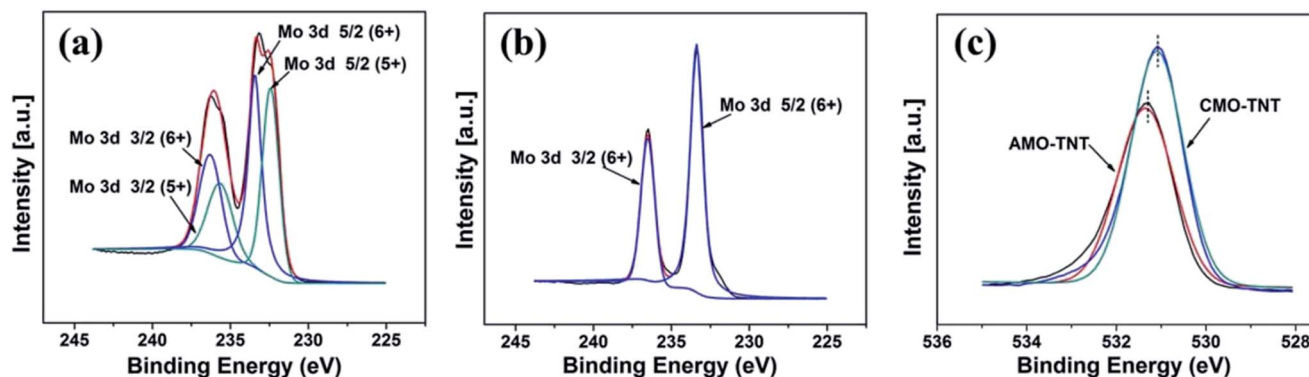


Fig. 4 XPS spectra in the Mo 3d binding energy region of AMO-TNT (a), CMO-TNT (b), and O 1s XPS spectra taken from samples AMO-TNT and CMO-TNT (c).



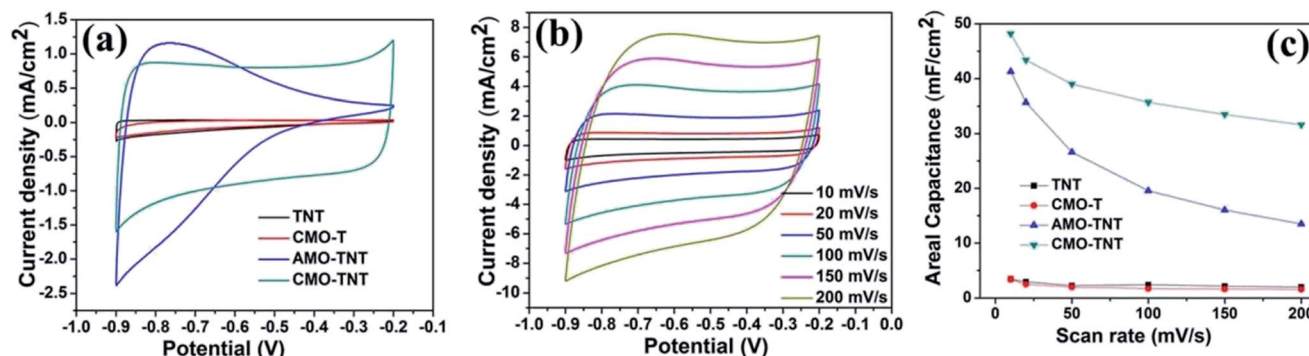


Fig. 5 The CV plots at a scan rate of  $20 \text{ mV s}^{-1}$  (a) for TNT, CMO-T, AMO-TNT, and CMO-TNT, the CV plots at different scan rates for CMO-TNT (b), and areal capacitances of the samples measured as a function of scan rate (c).

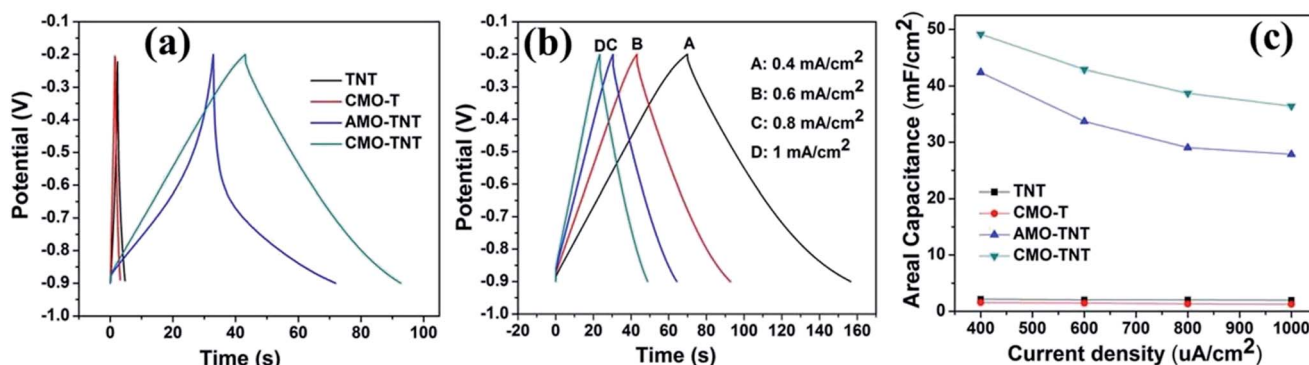


Fig. 6 The galvanostatic charge–discharge curves at a current density of  $0.6 \text{ mA cm}^{-2}$  for TNT, CMO-T, AMO-TNT, and CMO-TNT (a), galvanostatic charge–discharge curves for CMO-TNT achieved from  $0.4 \text{ mA cm}^{-2}$  to  $1 \text{ mA cm}^{-2}$  (b), the average areal capacitance at different current densities (c).

of the coated layer compared to the planar Ti substrate. In conclusion, it is the combined effect of TNTs and  $\text{MoO}_3$  layer that improves electrochemical properties of CMO-TNT.

Galvanostatic CD tests, which were performed in the potential range from  $-0.9$  to  $-0.2 \text{ V}$ , were also used to characterize the electrochemical properties and specific capacitance of the composite electrodes. From Fig. 6a, AMO-TNT and CMO-TNT exhibit longer charge/discharge time compared to TNT, indicating enhanced electrochemical performance. The results also indicate that the combination of TNTs and  $\alpha\text{-MoO}_3$  can enhance the electrochemical performance and increase specific capacitance. Fig. 6b presents the galvanostatic CD plots of CMO-TNT. The curves keep linear and symmetric at different current densities, which typically are the characteristic of double layer capacitance. Areal capacitances of the electrodes can be calculated from the galvanostatic CD curves using the following equation:

$$C_s = [I \times \Delta t] / [S \times \Delta V] \quad (2)$$

where  $I$  is discharge current,  $\Delta t$  discharge time,  $S$  the surface area,  $\Delta V$  the potential window. Fig. 6c shows the average areal capacitance at different current densities. The areal capacitances of TNT, CMO-T, AMO-TNT, and CMO-TNT are  $2.04 \text{ mF cm}^{-2}$ ,  $1.45 \text{ mF cm}^{-2}$ ,  $33.70 \text{ mF cm}^{-2}$ , and  $42.89 \text{ mF cm}^{-2}$  at a current density of  $0.6 \text{ mA cm}^{-2}$ , respectively.

The sample CMO-TNT possesses the largest specific capacitance than that of the other samples, which is agreed with the results of CV tests. Fig. 6c also shows the trends of areal capacitance as the current densities increase from  $0.4$  to  $1 \text{ mA cm}^{-2}$ . At low current densities, the inner active sites or the pores of the electrode can be fully accessed and diffused with cations. Therefore, high areal capacitance values are obtained.

To further understand electrochemical behavior of composite electrode materials, EIS measurements were carried out over a frequency range of  $0.01 \text{ Hz}$  to  $100 \text{ kHz}$ . Fig. 7 shows the Nyquist plots of TNT, CMO-T, AMO-TNT, and CMO-TNT. The high frequency region of the spectra is shown as the inset. Semicircular arcs are observed in the samples of TNT, CMO-T, and AMO-TNT, indicating poor charge transfer performance due to the interfacial transfer resistance between the electrode and electrolyte systems. However, no such a semi-circular arc for CMO-TNT is observed, indicating good charge transport capability. The high surface area and unique structure of the CMO-TNT electrode could explain the decrease in charge transfer resistance. These results indicate better capacitance performance of the CMO-TNT electrode.

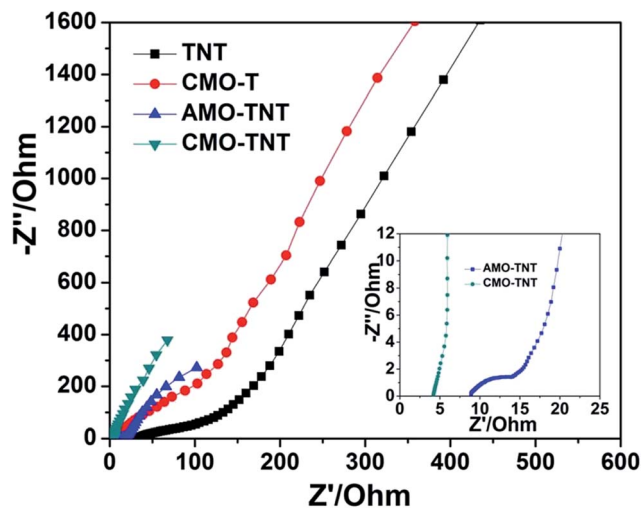


Fig. 7 Nyquist plots of TNT, CMO-T, AMO-TNT, and CMO-TNT.

The CMO-TNT electrode was measured at the current density of  $0.6 \text{ mA cm}^{-2}$  for 3000 cycles, to study its long-term capability. As shown in Fig. 8, the overall capacitance retention of CMO-TNT is about 51.7% after 3000 cycles. Interestingly, there is significant capacitance reduction ( $\sim 12\%$ ) in first 50 cycles. However, the capacitance fading rate of later cycle numbers becomes much lower than that of first 50 cycles. Fig. S5a and S5b† show SEM image and EDS spectrum of the sample achieved by galvanostatic CD testing of CMO-TNT for 50 cycles, respectively. A large number of pores are appeared, which is different from the top view of CMO-TNT (Fig. 3c). The EDS spectrum shows that the amount of Mo element after galvanostatic CD testing for 50 cycles is just 8.9%, which is lower than that of CMO-TNT (16.44%). These results indicate poor adhesion of  $\text{MoO}_3$  nanoplates to nanotube substrate, and thus detachment to a certain degree from nanotube surface over cycling. The XPS

survey spectrum confirms the formation of  $\text{MoO}_2$  after galvanostatic CD testing for 50 cycles (Fig. S6†). Wang *et al.*<sup>30</sup> reported that the presence of  $\text{MoO}_2$  reasonably reduces the electrochemical reactivity of molybdenum oxides, leading to a rapid capacity decay in the initial cycles. Taking these results into consideration, the rapid capacity decay may be ascribed to the detachment of  $\text{MoO}_3$  nanoplates from nanotube surface and the formation of  $\text{MoO}_2$  in the first 50 cycles. Additionally, above electrochemical analysis suggests the existence of intercalation and deintercalation of cations. On the one hand, the intercalated Na ion could occupy some active sites, leading to the decrease of capacitance.<sup>51</sup> On the other hand, the rapid capacity reduction of composite electrode is caused by the irreversible structure destruction resulting from the  $\text{Na}^+$  insertion.<sup>42,51,52</sup> With the increasing cycle numbers, some Na ions are introduced to Mo–O interlayers, which effectively inhibits the irreversible phase transition and stabilize the layer structure.<sup>51</sup> Thus, capacitance fading is greatly alleviated. Although our composite electrode has somewhat large capacitance loss, the final capacitance ( $21.72 \text{ mF cm}^{-2}$ ) after 3000 continuous charge–discharge cycles is still higher than the initial capacitance ( $2.50\text{--}20.08 \text{ mF cm}^{-2}$ ) reported in literatures.<sup>53–57</sup>

## 4. Conclusion

In our study, highly ordered  $\text{TiO}_2$  nanotube arrays were synthesized by one-step anodization and then annealed at  $450^\circ\text{C}$  in air to achieve crystalline phase, which worked as active surface coated with  $\text{MoO}_3$  through electrochemical deposition. The resulting CMO-TNT electrode shows a large area capacitance of  $43.42 \text{ mF cm}^{-2}$  at a scan rate of  $20 \text{ mV s}^{-1}$ . The enhanced electrochemical properties are attributed to combined effect of the  $\text{TiO}_2$  nanotube arrays and  $\text{MoO}_3$  layer. The results suggest that  $\text{TiO}_2$  nanotube coated with crystalline  $\alpha\text{-MoO}_3$  film can be used as a promising electrode material.

## Acknowledgements

The authors are very much grateful to the National Engineering Research Center for Biomaterials, Sichuan University for the assistance with the microscopy work. S. P. Sun thanks to Mr Yan for his encouragement and support during the research.

## References

- 1 Y. Liu, X. Y. Cai, J. H. Jiang, M. Yan and W. D. Shi, *Appl. Surf. Sci.*, 2017, **396**, 774–779.
- 2 P. Bhojane, S. Sen and P. M. Shirage, *Appl. Surf. Sci.*, 2016, **377**, 376–384.
- 3 C. N. He, S. Wu, N. Q. Zhao, C. S. Shi, E. Z. Liu and J. J. Li, *ACS Nano*, 2013, **7**, 4459–4469.
- 4 G. Q. Zhang, L. Yu, H. B. Wu, H. E. Hoster and X. W. Lou, *Adv. Mater.*, 2012, **24**, 4609–4613.
- 5 M. P. A. Muthalif, Y.-S. Lee, C. D. Sunesh, H.-J. Kim and Y. Choe, *Appl. Surf. Sci.*, 2017, **396**, 582–589.
- 6 B. Filanovsky, E. Granot, R. Dirawi, I. Presman, I. Kuras and F. Patolsky, *Nano Lett.*, 2011, **11**, 1727–1732.

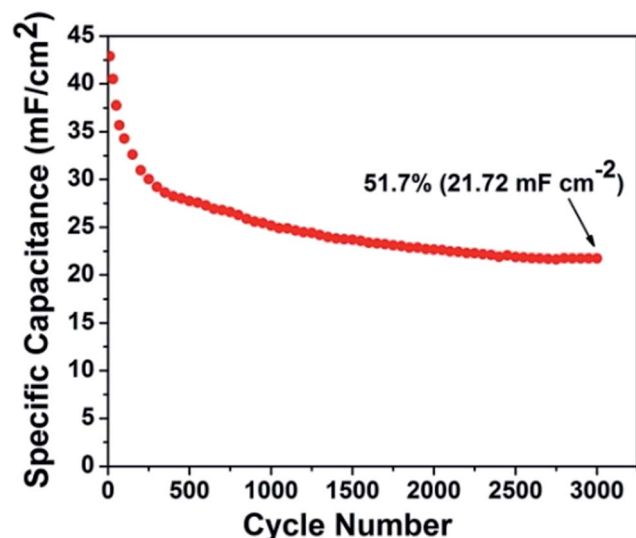


Fig. 8 Cyclic performance of CMO-TNT composite electrode at a current density of  $0.6 \text{ mA cm}^{-2}$ .





- 7 C. Kim, *J. Power Sources*, 2005, **142**, 382–388.
- 8 C. Merino, P. Soto, E. Vilaplana-Ortego, J. M. G. d. Salazar, F. Pico and J. M. Rojo, *Carbon*, 2005, **43**, 551–557.
- 9 A. Izadi-Najafabadi, T. Yamada, D. N. Futaba, M. Yudasaka, H. Takagi, H. Hatori, S. Iijima and K. Hata, *ACS Nano*, 2011, **5**, 811–819.
- 10 P. Chen, H. T. Chen, J. Qiu and C. W. Zhou, *Nano Res.*, 2010, **3**, 594–603.
- 11 Z. J. Fan, J. Yan, L. J. Zhi, Q. Zhang, T. Wei, J. Feng, M. L. Zhang, W. Z. Qian and F. Wei, *Adv. Mater.*, 2010, **22**, 3723–3728.
- 12 L. L. Zhang, R. Zhou and X. S. Zhao, *J. Mater. Chem.*, 2010, **20**, 5983–5992.
- 13 C.-C. Hu, K.-H. Chang, M.-C. Lin and Y.-T. Wu, *Nano Lett.*, 2006, **6**, 2690–2695.
- 14 K.-M. Lin, K.-H. Chang, C.-C. Hu and Y.-Y. Li, *Electrochim. Acta*, 2009, **54**, 4574–4581.
- 15 L. H. Cui, Y. Wang, X. Shu, J. F. Zhang, C. P. Yu, J. W. Cui, H. M. Zheng, Y. Zhang and Y. C. Wu, *RSC Adv.*, 2016, **6**, 12185–12192.
- 16 F. Gobal and M. Faraji, *Electrochim. Acta*, 2013, **100**, 133–139.
- 17 S. S. Zhu, P. P. Zhang, L. Chang, Y. Zhong, K. Wang, H. B. Shao, J. M. Wang, J. Q. Zhang and C.-N. Cao, *Phys. Chem. Chem. Phys.*, 2016, **18**, 8529–8536.
- 18 H. Zhou and Y. R. Zhang, *J. Power Sources*, 2014, **272**, 866–879.
- 19 R. S. Ray, B. Sarma, A. L. Jurovitzki and M. Misra, *Chem. Eng. J.*, 2015, **260**, 671–683.
- 20 B. Sarma, R. S. Ray and M. Misra, *Mater. Lett.*, 2015, **139**, 77–80.
- 21 Y. B. Xie, D. Wang, Y. Z. Zhou, H. X. Du and C. Xia, *Synth. Met.*, 2014, **198**, 59–66.
- 22 H. X. Du, Y. B. Xie, C. Xia, W. Wang and F. Tian, *New J. Chem.*, 2014, **38**, 1284–1293.
- 23 Y. Gao, Y. Z. Wang, X. Xu, K. Ding and D. M. Yu, *RSC Adv.*, 2014, **4**, 63719–63724.
- 24 K. Y. Xie, J. Li, Y. Q. Lai, Z. A. Zhang, Y. X. Liu, G. G. Zhang and H. T. Huang, *Nanoscale*, 2011, **3**, 2202–2207.
- 25 H. F. Su, T. Wang, S. Y. Zhang, J. M. Song, C. J. Mao, H. L. Niu, B. K. Jin, J. Y. Wu and Y. P. Tian, *Solid State Sci.*, 2012, **14**, 677–681.
- 26 R. Ren, Z. H. Wen, S. M. Cui, Y. Hou, X. R. Guo and J. H. Chen, *Sci. Rep.*, 2015, **5**, 10714.
- 27 T. Close, G. Tulsyan, C. A. Diaz, S. J. Weinstein and C. Richter, *Nat. Nanotechnol.*, 2015, **10**, 418–422.
- 28 J. Li and X. H. Liu, *Mater. Lett.*, 2013, **112**, 39–42.
- 29 M. Sarfraz, M. F. A. Aboud and I. Shakir, *J. Alloys Compd.*, 2015, **650**, 123–126.
- 30 Z. Y. Wang, S. Madhavi and X. W. Lou, *J. Phys. Chem. C*, 2012, **116**, 12508–12513.
- 31 P. Meduri, E. Clark, J. H. Kim, E. Dayalan, G. U. Sumanasekera and M. K. Sunkara, *Nano Lett.*, 2012, **12**, 1784–1788.
- 32 L. L. Cai, P. M. Rao and X. L. Zheng, *Nano Lett.*, 2011, **11**, 872–877.
- 33 D. Yao, M. R. Field, A. P. O'Mullane, K. Kalantar-zadeh and J. Z. Ou, *Nanoscale*, 2013, **5**, 10353–10359.
- 34 L. Q. Wang, P. Gao, D. Bao, Y. Wang, Y. J. Chen, C. Chang, G. B. Li and P. P. Yang, *Cryst. Growth Des.*, 2014, **14**, 569–575.
- 35 J. C. Park and H. Song, *Chem. Mater.*, 2007, **19**, 2706–2708.
- 36 M. F. Hassan, Z. P. Guo, Z. Chen and H. K. Liu, *J. Power Sources*, 2010, **195**, 2372–2376.
- 37 H. Li, P. Balaya and J. Maier, *J. Electrochem. Soc.*, 2004, **151**, A1878–A1885.
- 38 W. H. Zuo, W. H. Zhu, D. F. Zhao, Y. F. Sun, Y. Y. Li, J. P. Liu and X. W. (David) Lou, *Energy Environ. Sci.*, 2016, **9**, 2881–2891.
- 39 J. P. Liu, C. Guan, C. Zhou, Z. Fan, Q. Q. Ke, G. Z. Zhang, C. Liu and J. Wang, *Adv. Mater.*, 2016, **28**, 8732–8739.
- 40 C. Wang, L. X. Wu, H. Wang, W. H. Zuo, Y. Y. Li and J. P. Liu, *Adv. Funct. Mater.*, 2015, **25**, 3524–3533.
- 41 D. S. Guan, J. Y. Li, X. F. Gao and C. Yuan, *RSC Adv.*, 2014, **4**, 4055–4062.
- 42 B. Ahmed, M. Shahid, D. H. Nagaraju, D. H. Anjum, M. N. Hedhili and H. N. Alshareef, *ACS Appl. Mater. Interfaces*, 2015, **7**, 13154–13163.
- 43 M. L. Petrova, M. S. Bojinov and I. H. Gadjev, *Bulg. Chem. Commun.*, 2011, **43**, 60–63.
- 44 Y. B. Xie, Y. Wang and H. X. Du, *J. Mater. Sci. Eng. B*, 2013, **178**, 1443–1451.
- 45 R. B. Pujari, V. C. Lokhande, V. S. Kumbhar, N. R. Chodankar and C. D. Lokhande, *J. Mater. Sci.: Mater. Electron.*, 2016, **27**, 3312–3317.
- 46 I. Shakir and M. Sarfraz, *Electrochim. Acta*, 2014, **147**, 380–384.
- 47 J. Wang, J. Polleux, J. Lim and B. Dunn, *J. Phys. Chem. C*, 2007, **111**, 14925–14931.
- 48 S. Balendhran, J. K. Deng, J. Z. Ou, S. Walia, J. Scott, J. S. Tang, K. L. Wang, M. R. Field, S. Russo, S. Zhuikov, M. S. Strano, N. Medhekar, S. Sriram, M. Bhaskaran and K. Kalantar-zadeh, *Adv. Mater.*, 2013, **25**, 109–114.
- 49 C. V. Ramana, V. V. Atuchin, H. Groult and C. M. Julien, *J. Vac. Sci. Technol., A*, 2012, **30**, 04D105.
- 50 T. M. McEvoy and K. J. Stevenson, *Langmuir*, 2003, **19**, 4316–4326.
- 51 Y. F. Dong, X. M. Xu, S. Li, C. H. Han, K. N. Zhao, L. Zhang, C. J. Niu, Z. Huang and L. Q. Mai, *Nano Energy*, 2015, **15**, 145–152.
- 52 T. Tao, Q. Y. Chen, H. P. Hu and Y. Chen, *Mater. Lett.*, 2012, **66**, 102–105.
- 53 S. P. Sun, X. M. Liao, G. F. Yin, Y. D. Yao, Z. B. Huang and X. M. Pu, *J. Alloys Compd.*, 2016, **680**, 538–543.
- 54 H. Wu, D. D. Li, X. F. Zhu, C. Y. Yang, D. F. Liu, X. Y. Chen, Y. Song and L. F. Lu, *Electrochim. Acta*, 2014, **116**, 129–136.
- 55 L. X. Zheng, C. D. Wang, Y. C. Dong, H. D. Bian, T. F. Hung, J. Lu and Y. Y. Li, *Appl. Surf. Sci.*, 2016, **362**, 399–405.
- 56 Z. Li, Y. T. Ding, W. J. Kang, C. Li, D. Lin, X. Y. Wang, Z. W. Chen, M. H. Wu and D. Y. Pan, *Electrochim. Acta*, 2015, **161**, 40–47.
- 57 H. Zhou and Y. R. Zhang, *J. Phys. Chem. C*, 2014, **118**, 5626–5636.

